Large-eddy simulation of a free round jet using multifractal subgrid-scale modeling

By G.C. Burton

1. Motivation and objectives

The free round turbulent jet is perhaps the most extensively studied of the canonical free-shear turbulent flows. Turbulent jets are important to a variety of industrial applications such as fuel injectors, furnaces, and rocket engines. Owing to the difficulty, time and expense of conducting experimental studies of most turbulent flows, numerical simulation of the turbulent jet has been increasingly used to guide design and development work at the industrial level. It has also provided numerous insights into fundamental physical laws governing such flows. Reynolds-averaged Navier-Stokes (RANS) studies of such jets, in which only the time-averaged mean flow is explicitly calculated, have been used extensively in the past, but remain of only limited accuracy, and thus of limited usefulness, in the industrial design process. On the other hand, fully resolved studies (DNS) of turbulent flows, which could provide the needed precision, will remain for most flows encountered in engineering practice far beyond the capability of the most powerful computers for some decades to come. Midway between DNS and RANS lies the approach of large-eddy simulation (LES), which explicitly calculates the large-scale turbulent structures, while modeling the smaller unresolved scales. An accurate model for the small scales is needed for LES to provide a reliably accurate tool for practical turbulent flow problems. Most current models rely on an eddy-viscosity assumption that the smallest-resolved eddies in an LES remove energy from the resolved flow much like molecular viscosity at the smallest continuous scales in actual turbulence. Such models, even if roughly capturing the integrated transfer of energy to the subgrid scales, cannot reproduce the detailed spatial structure of the true energy transfer field $\mathcal{P}(x,t)$.

Recently Burton & Dahm (2004 *a,b*) have proposed a multifractal subgrid-scale model that does not rely on an eddy-viscosity assumption, but instead is derived from the multifractal structure of the vorticity field in high Reynolds-number turbulence. From this, a new, highly accurate model for the subgrid velocity field u_i^{sgs} has been proposed that permits explicit calculation of the nonlinear term $\overline{u_i\,u_j}$, thus closing the filtered Navier-Stokes equations. Prior LES of forced homogeneous isotropic turbulence using the multifractal model indicate that stable and remarkably accurate simulations may be obtained, including recovery of the detailed spatial structure of the subgrid energy-production field $\mathcal{P}^{sgs}(\mathbf{x},t)$, with $\rho \geq 0.995$ (Burton & Dahm 2004*b*). The work reported in the present paper involves refining and evaluating the accuracy of the multifractal model in the significantly more complex configuration of a free round turbulent jet.

2. Overview: Multifractal subgrid-scale modeling

A full development of multifractal subgrid-scale modeling for LES is given in Burton & Dahm (2004 *a,b*). Only the most important aspects of the modeling approach are summarized here.

2.1. *The subgrid-scale model*

Multifractal modeling derives a representation for the subgrid velocity field $\mathbf{u}^{sgs}(\mathbf{x},t)$ from a representation of the subgrid vorticity field $\boldsymbol{\omega}^{sgs}(\mathbf{x},t)$ using the Biot-Savart operator. The resulting subgrid velocity field is then used to solve explicitly the subgrid stress tensor τ_{ij}^* using the form of the filtered momentum equation given by

$$\frac{\partial \overline{u}_i}{\partial t} + \frac{\partial}{\partial x_j}\overline{\overline{u}_i\,\overline{u}_j} + \frac{1}{\rho}\frac{\partial \overline{p}}{\partial x_i} - \nu\frac{\partial^2 \overline{u}_i}{\partial x_j^2} = -\frac{\partial}{\partial x_j}\tau_{ij}^*, \tag{2.1}$$

where

$$\tau_{ij}^* \equiv \overline{\overline{u}_i\, u_j^{sgs}} + \overline{u_i^{sgs}\,\overline{u}_j} + \overline{u_i^{sgs}\, u_j^{sgs}}. \tag{2.2}$$

The derivation begins by noting that the enstrophy field $\frac{1}{2}\,\boldsymbol{\omega}\cdot\boldsymbol{\omega}(\mathbf{x},t)$ in high Reynolds number turbulence exhibits multifractal scale similarity over inertial range scales. Therefore, the spatial distribution of subgrid vorticity magnitude $|\boldsymbol{\omega}^{sgs}|(\mathbf{x},t)$ may be described by a multiplicative multifractal cascade. Similarly, DNS data indicates that the distribution of subgrid vorticity orientations $\mathbf{e}^{\boldsymbol{\omega}^{sgs}}(\mathbf{x},t)$ may be represented by an additive orientation cascade by which the subgrid vorticity field decorrelates isotropically from the smallest resolved field $\boldsymbol{\omega}^{\Delta}(\mathbf{x},t)$. The subgrid velocity field $\mathbf{u}^{sgs}(\mathbf{x},t)$ may then be determined by applying the Biot-Savart operator to this representation of the subgrid vorticity field. Since both the magnitude and orientation cascades are stochastic in nature, the resulting integral can be evaluated using probabilistic concepts with the result that the subgrid stress tensor τ_{ij}^* may be modeled as

$$\tau_{ij}^* \approx \mathcal{B}\left(\overline{\overline{u}_i\, u_j^{\Delta}} + \overline{\overline{u}_j\, u_i^{\Delta}}\right) + \mathcal{B}^2\,\overline{u_i^{\Delta}\, u_j^{\Delta}}, \tag{2.3}$$

where

$$\mathcal{B} \equiv 0.47\; 2^{-\frac{2\mathcal{N}}{3}}\left[2^{\frac{4\mathcal{N}}{3}} - 1\right]^{\frac{1}{2}}, \tag{2.4}$$

$\mathcal{N}$ represents the number of cascade iterations within the subgrid field given by

$$\mathcal{N} \equiv \log_2(\Delta/\lambda_\nu). \tag{2.5}$$

and where u_i^{Δ} is the velocity field associated with the smallest resolved scale Δ. This involves only quantities available from the resolved scales of the flow, thus closing the subgrid-stress term in the momentum equation in (2.1).

Each of the filtered products represented by the long overbars in (2.3) is explicitly evaluated as

$$\overline{\overline{u}_i\, u_j^{\Delta}} \approx \frac{1}{\Delta^3}\int_{\Delta^3} \mathcal{G}_i(\mathbf{x})\,\mathcal{H}_j(\mathbf{x})\,d^3\mathbf{x} \tag{2.6}$$

$$\overline{u_i^{\Delta}\, u_j^{\Delta}} \approx \frac{1}{\Delta^3}\int_{\Delta^3} \mathcal{H}_i(\mathbf{x})\,\mathcal{H}_j(\mathbf{x})\,d^3\mathbf{x}, \tag{2.7}$$

and the filtered product of the resolved velocity components in (2.1) is similarly evaluated as

$$\overline{\overline{u}_i\,\overline{u}_j} \approx \frac{1}{\Delta^3}\int_{\Delta^3} \mathcal{G}_i(\mathbf{x})\,\mathcal{G}_j(\mathbf{x})\,d^3\mathbf{x}. \tag{2.8}$$

The functions $\mathcal{G}_i(\mathbf{x})$ and $\mathcal{H}_i(\mathbf{x})$ are, respectively, Legendre expansions of $\overline{u}_i(\mathbf{x})$ and $u_i^{\Delta}(\mathbf{x})$

as

$$\overline{u}_i(\mathbf{x}) \approx \sum_{l,m,n} a_{lmn}\, \Phi_l(x)\, \Phi_m(y)\, \Phi_n(z) \equiv \mathcal{G}_i(\mathbf{x}) \tag{2.9}$$

$$u_i^{\Delta}(\mathbf{x}) \approx \sum_{l,m,n} b_{lmn}\, \Phi_l(x)\, \Phi_m(y)\, \Phi_n(z) \equiv \mathcal{H}_i(\mathbf{x}), \tag{2.10}$$

where the required cell-centered values of u_i^{Δ} are obtained from the cell-centered values of $\overline{u}_i(\mathbf{x})$ as

$$u_i^{\Delta} \equiv \overline{u}_i - a_{000}. \tag{2.11}$$

Equations (2.1) and (2.3) – (2.11) give a complete statement of the multifractal model for large-eddy simulation.

2.2. *Backscatter limiting*

Numerical errors introduced in the resolved scales during an actual simulation are reduced by introducing an explicit backscatter limiter in the flow calculation. This effectively decouples the role of the subgrid model from the additional burden of controlling the numerical error. The backscatter limiting is implemented by a small reduction in the local magnitude of only those stress components that contribute to local backscatter of energy from the subgrid scales to the resolved scales. Since $\mathcal{P} \equiv \mathcal{P}^* + \mathcal{P}^R$, where

$$\mathcal{P}^*(\mathbf{x},t) \equiv -\tau_{ij}^*\, \overline{S}_{ij} \tag{2.12}$$

and

$$\mathcal{P}^R(\mathbf{x},t) \equiv -\overline{\overline{u}_i\, \overline{u}_j}\, \overline{S}_{ij}, \tag{2.13}$$

the limiter first calculates each of the terms $\mathcal{P}_{(ij)}$ that contribute to the local subgrid production as

$$\mathcal{P}_{(ij)} \equiv -\left(\overline{\overline{u}_{(i)}\, \overline{u}_{(j)}} + \tau_{(ij)}^*\right) \overline{S}_{(ij)}\,, \tag{2.14}$$

where the subscript parentheses indicate that no summation is implied. Any of the local $\mathcal{P}_{(ij)}$ terms that are negative will contribute to local backscatter of energy, and thus only those terms are reduced as

$$\widehat{\mathcal{P}_{(ij)}} \equiv (1 - C_{\mathcal{B}})\, \mathcal{P}_{(ij)}\,, \tag{2.15}$$

where $0 \le C_{\mathcal{B}} \le 1$ is a prescribed backscatter-limiter coefficient. This has the effect of locally reducing the contribution to backscatter into the resolved scales by the amount $C_{\mathcal{B}}\, \mathcal{P}_{(ij)}$, which is largest where $\mathcal{P}_{(ij)}$ is most strongly negative and thus where the numerical errors are presumably also largest.

To implement this in the momentum equation in (2.1), for each (ij) in (2.14) for which $\mathcal{P}_{(ij)} < 0$, the corresponding production term $\mathcal{P}_{(ij)}$ is effectively replaced with $\widehat{\mathcal{P}_{(ij)}}$ from (2.15), by replacing the corresponding $\overline{\overline{u}_{(i)}\, \overline{u}_{(j)}}$ in (2.1) with the backscatter-limited value

$$\widehat{\overline{\overline{u}_{(i)}\, \overline{u}_{(j)}}} = (1 - C_{\mathcal{B}})\, \overline{\overline{u}_{(i)}\, \overline{u}_{(j)}}, \tag{2.16}$$

and replacing the corresponding $\tau_{(ij)}^*$ in (2.1) with the backscatter-limited value

$$\widehat{\tau_{(ij)}^*} = (1 - C_{\mathcal{B}})\, \tau_{(ij)}^*. \tag{2.17}$$

Altering the components in the momentum equation in this manner is equivalent to backscatter-limiting the subgrid energy production field $\mathcal{P}(\mathbf{x},t)$ as in (2.15). Note that the

limiter procedure could alternatively be implemented by an analogous forward-transfer accelerator, in which the backscatter reduction is replaced by a forward-transfer accelerator factor $(1 + C_{\mathcal{F}})$ for each (ij) in (2.14) for which $\mathcal{P}_{(ij)} > 0$.

3. Adaptive backscatter limiting for LES

3.1. *Motivation*

Prior studies have indicated that a backscatter reduction factor of $C_{\mathcal{B}} \approx 0.15$ provides reasonably optimal control of resolved energy levels for the specific case of periodic forced homogeneous isotropic turbulence for a resolution of $N = 32^3$ and a grid-cell Reynolds number of $Re_{\Delta} \approx 160$ (Burton & Dahm 2004*b*). However, in the more complex configurations seen in practical engineering development work such as the turbulent round jet, spatial and temporal variation in flow conditions may be significant during the simulation. As a result, it may prove advantageous to vary the value for $C_{\mathcal{B}}$ during the simulation. Thus before the multifractal model was used in an LES of a round jet, a method was developed and tested for adaptively determining the value for the backscatter coefficient $C_{\mathcal{B}}$. This adaptive approach is shown to eliminate globally numerical errors in subgrid-energy transfer during a simulation or to reduce local errors to the order of the spatial derivative operators.

3.2. *Resolved energy transport*

The kinetic energy of the resolved velocity field $\mathcal{E}(\mathbf{x},t) \equiv \frac{1}{2}\overline{u}_i\overline{u}_i$, as implemented in the multifractal model evolves according to

$$\frac{\partial}{\partial t}\,\mathcal{E}(\mathbf{x},t) \;=\; \frac{\partial}{\partial x_j}\,[\,\mathcal{R}_j\,] \;-\; \mathcal{D} \;-\; \mathcal{P}. \tag{3.1}$$

The flux vector $\mathcal{R}_j$ is given by

$$\mathcal{R}_j(\mathbf{x},t) \;\equiv\; -\left[\,\overline{u}_i\,\left(\,\overline{\overline{u}_i\,\overline{u}_j} \;+\; \tau^*_{ij}\,\right) \;+\; \overline{u}_i\,\frac{\overline{p}}{\rho}\,\delta_{ij} \;-\; \nu\,\frac{\partial\,\mathcal{E}}{\partial x_j}\,\right], \tag{3.2}$$

which appears in (3.1) in divergence form and thus has no effect on energy transfer between the resolved and subgrid scales. Only the resolved viscous dissipation $\mathcal{D}$ defined as

$$\mathcal{D}(\mathbf{x},t) \;\equiv\; 2\nu\,\overline{S}_{ij}\,\overline{S}_{ij} \tag{3.3}$$

and the subgrid energy production $\mathcal{P}$ defined as

$$\mathcal{P}(\mathbf{x},t) \;\equiv\; -\,\left(\,\overline{\overline{u}_i\,\overline{u}_j} \;+\; \tau^*_{ij}\,\right)\,\overline{S}_{ij}, \tag{3.4}$$

contribute to the exchange of energy between the resolved and subgrid scales. The subgrid production $\mathcal{P}$ in (3.4) may be broken down further into components contributing to the forward transfer of energy $\mathcal{P}^{\,forw}$ where,

$$\mathcal{P}^{forw} = \sum \mathcal{P}_{(ij)} \quad \forall\, \mathcal{P}_{(ij)} > 0 \tag{3.5}$$

and backscatter $\mathcal{P}^{\,back}$ where

$$\mathcal{P}^{back} = \sum \mathcal{P}_{(ij)} \quad \forall\, \mathcal{P}_{(ij)} < 0 \tag{3.6}$$

and where in (3.1)

$$\mathcal{P}(\mathbf{x},t) \;\equiv\; \mathcal{P}^{forw}(\mathbf{x},t) \;+\; \mathcal{P}^{\,back}(\mathbf{x},t)\,. \tag{3.7}$$

This gives the final energy transport equation as

$$\frac{\partial}{\partial t}\,\mathcal{E}(\mathbf{x},t) \;=\; \frac{\partial}{\partial x_j}\,[\,\mathcal{R}_j\,] \;-\; \mathcal{D} \;-\; \left(\mathcal{P}^{forw} + \mathcal{P}^{\,back}\right). \tag{3.8}$$

3.3. *Implementation of adaptive backscatter limiter*

We can however adaptively select a local backscatter reduction coefficient $C_{\mathcal{B}}(\mathbf{x},t)$ as follows. Equation 3.8 with the backscatter limiter can be stated as

$$\frac{\partial}{\partial t}\,\mathcal{E}(\mathbf{x},t) \;=\; \frac{\partial}{\partial x_j}\,[\,\mathcal{R}_j\,] \;-\; \mathcal{D} \;-\; \left(\mathcal{P}^{forw} + (\,1 \;-\; C_{\mathcal{B}})\;\mathcal{P}^{\,back}\right). \tag{3.9}$$

with all terms similarly defined as in the previous section. First, a target value is selected for energy transfer at a given location, which is taken to be the exact amount of resolved energy desired at a particular location at the next timestep as $\mathcal{E}^{exact}(\mathbf{x},t) \equiv \mathcal{E}^{(n+1)}(\mathbf{x},t)$. This target value may be taken from the value predicted by the multifractal subgrid model itself or from some other estimate, such as for example that predicted by the dynamic Smagorinsky model. With an initial guess for the coefficient as $C_{\mathcal{B}}^{(n)}$, the flow solver is then advanced one step in time giving an estimated new value for the resolved energy $\mathcal{E}^{*}$ as

$$\mathcal{E}^{(*)}(\mathbf{x},t) \;=\; \mathcal{E}^{(n)} \;+\; \Delta t\left[\frac{\partial}{\partial x_j}\,[\,\mathcal{R}_j\,] \;-\; \mathcal{D} \;-\; \mathcal{P}^{forw} - \beta\left(1 \;-\; C_{\mathcal{B}}^{(n)}\right)\,\mathcal{P}^{\,back}\right]^{(n)}, \tag{3.10}$$

where β is a relaxation factor, that may nominally be set to $\beta \;=\; 1$. Note, however, that in general the resulting value $\mathcal{E}^{(*)}(\mathbf{x},t) \neq \mathcal{E}^{exact}(\mathbf{x},t)$, due to the effect of numerical errors such as aliasing. Therefore, the error between this actual and the intended final kinetic energy is defined as

$$\epsilon \;\equiv\; \mathcal{E}^{(*)}(\mathbf{x},t) \;-\; \mathcal{E}^{exact}(\mathbf{x},t). \tag{3.11}$$

Usually $\epsilon \;>\; 0$, although this need not be the case. The numerical error now may be eliminated by adjusting the backscatter coefficient $C_{\mathcal{B}}$ in (3.10) through an iterative scheme described below. First, a new value for the coefficient for the next iteration is determined as

$$C_{\mathcal{B}}^{(n+1)} \;=\; C_{\mathcal{B}}^{(n)} + \Delta\, C_{\mathcal{B}}, \tag{3.12}$$

where

$$\Delta\, C_{\mathcal{B}}^{(n+1)} \equiv \frac{\epsilon}{\mathcal{P}^{back}}, \tag{3.13}$$

with ϵ and $\mathcal{P}^{back}$ as defined above. Using the new value $C_{\mathcal{B}}^{(n+1)}$, the estimated new energy may be calculated according to (3.10). This will produce an updated value for the energy transfer error ε in (3.11). The iteration scheme thus consists of iterating on the backscatter coefficient $C_{\mathcal{B}}^{(n)}$ value, as defined above until $\varepsilon \;\to\; 0$. This method is essentially a Newton-Raphson iterative scheme with

$$x^n \;-\; \frac{F(x^n)}{F'(x^n)} \;=\; x^{n+1}, \tag{3.14}$$

where the backscatter coefficient provides

$$x^n \;\equiv\; C_{\mathcal{B}}^{(n)}\,, \tag{3.15}$$

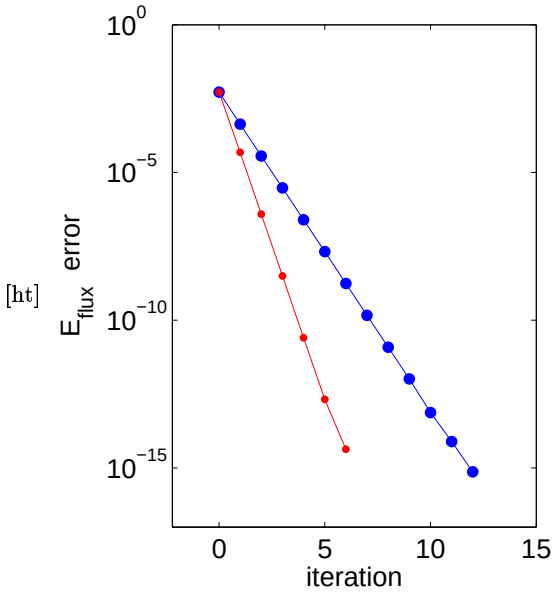

FIGURE 1. Rapid convergence to machine zero is evident for the iterative method described in this paper. (*Large dots:*) iteration with no relaxation. (*Small dots:*) iteration with small relaxation factor $\beta = 1.01$.

and the error in the final kinetic energy provides

$$F(x) \equiv \epsilon. \tag{3.16}$$

It can be shown that the iteration scheme converges to a unique solution if $C_{\mathcal{B}}^o$ is selected even with only marginal accuracy. Studies run to date indicate that iteration with some relaxation will very quickly drive $\epsilon \to 0$, as indicated in Fig. 1, below. The present method applies to the solution for a single global value of $C_{\mathcal{B}}$, in which all flux terms $\mathcal{R}_j$ in (3.10) sum to zero at the domain boundaries according to Gauss' theorem. The method also applies to a solver which employs a collocated storage arrangement for primitive flow variables, so that a unique value for the kinetic energy of the resolved scales can be determined in each computational control volume. If the scheme is used to solve for such a local value, the iteration scheme will only converge to the order of the error of the flux term.

On a staggered grid, in which separate control volumes are defined for each primitive flow variable (Harlow & Welch 1965), the method in (3.10) must be modified so that separate iterative systems are solved simultaneously for components of kinetic energy in each of the three coordinate directions. The transport equation for the i-th component contribution to kinetic energy is then given by

$$\frac{\partial}{\partial t}\,\mathcal{E}_i\,(\mathbf{x},t) \;=\; \frac{\partial}{\partial x_j}\left[\,\mathcal{R}_{(i)j}\,\right] \;-\; \mathcal{D}_i \;-\; \mathcal{P}_i \;-\; \mathcal{W}_i. \tag{3.17}$$

where $\mathcal{R}_{(i)j}$ is the i-th component of the flux vector in (3.2), and $\mathcal{D}_i$ and $\mathcal{P}_i$ are those portions of the dissipation and subgrid production fields that involve the i-th components of the fields in (3.3) and (3.4), respectively. The term $\mathcal{W}_i$ involves the interaction of the

stress field $\overline{u_i\, u_j}$ with the i-th components of the rotation tensor Ω_{ij} as

$$\mathcal{W}_i \;\equiv\; \overline{u_{(i)}\, u_j}\, \Omega_{(i)j} \tag{3.18}$$

where the rotation tensor is given by

$$\Omega_{ij} \;\equiv\; \frac{1}{2}\left(\frac{\partial u_j}{\partial x_i} - \frac{\partial u_i}{\partial x_j}\right) \tag{3.19}$$

and where the parentheses in (3.18) again indicate that summation is not implied over the particular component direction. The term in (3.18) accounts for solid-body rotation within the fluid that moves kinetic energy from one component direction to another. The iteration scheme of (3.10) on a staggered grid is then given as

$$\mathcal{E}_i^{(*)}(\mathbf{x},t) \;=\; \mathcal{E}_i^{(n)} \;+\; \Delta t\left[\frac{\partial}{\partial x_j}\left[\,\mathcal{R}_{(i)j}\,\right] \;-\; \mathcal{D}_i \;-\; \mathcal{W}_i \;-\; \mathcal{P}_i^{forw} - \left(1 \;-\; C_{\mathcal{B}}^{(n)}\right)\,\mathcal{P}_i^{back}\right]^{(n)}. \tag{3.20}$$

4. Differential backscatter limiting

The backscatter-limiter methodology has also been modified to more precisely capture the transfer of energy across all the resolved scales in the flow. This modification makes use of the significant information about the stress field contained in the product of the Legendre expansions in (2.6) – (2.8), and involves applying a backscatter reduction factor that varies with the order of each term within the Legendre product expansions.

4.1. *Overview of approach*

Because the multifractal model calculates the inertial stresses in (2.6) – (2.8) as volume integrals of the products of the Legendre expansions of the velocity component fields, the model simply consists of a linear summation of monomial terms. Thus, for example the cross-term stress in (2.6) can be expressed as

$$\overline{\overline{u}_i\, u_j^{\Delta}} \;\equiv\; \frac{1}{\Delta^3}\int_{\Delta^3}\sum_{n=1}^{N}\gamma_n\,\left(x_i^{(a)}x_j^{(b)}x_k^{(c)}\right)_n\,d\mathbf{x}^3, \tag{4.1}$$

where $(a),(b),(c)$ are the exponents representing the order of the term in each component direction, and γ represents the coefficient of the particular monomial term, with similar expressions for (2.7) and (2.8). Since the integration in (4.1) is symmetric about the canonical Legendre interval $I = [\,-1,\,1\,]$, odd-order (antisymmetric) terms will vanish in the integration. Thus the summation in (4.1) involves terms containing various combinations of constant, 2nd, and 4th order variables in each of the three coordinate directions x_i. Note also that any 4th order term appearing in (4.1) is generated only through the multiplication of the Legendre expansions and cannot arise directly from the Legendre expansions in (2.9) and (2.10) themselves, which of course contain basis functions up to second order. Such 4th-order terms correspond to aliased frequencies within the product summation.

4.2. *Implementation of differential backscatter limiting*

Rather than applying a constant backscatter-reduction coefficient $C_{\mathcal{B}}$ to all terms in (4.1) as has been done previously (Burton & Dahm 2004), the present approach instead applies different $C_{\mathcal{B}}$ reduction factors to individual summation terms depending on the order of the given term in (4.1). A number of variations were evaluated to determine

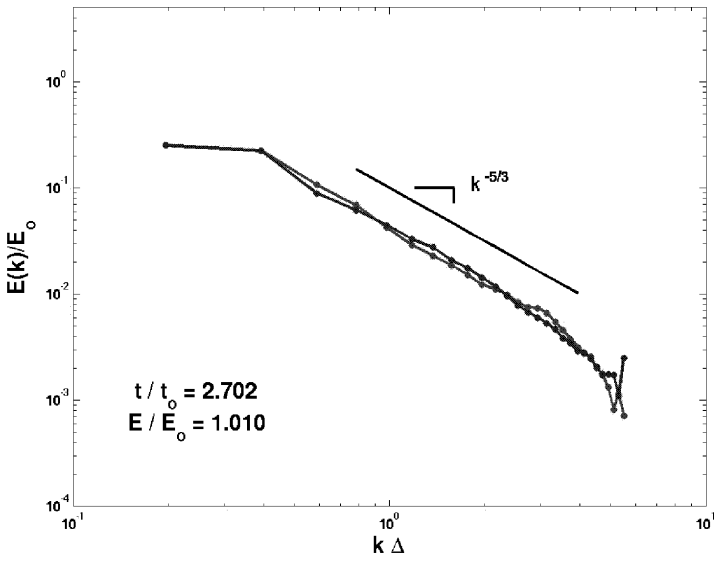

FIGURE 2. Resolved energy spectrum $E(k)$ from LES of forced, periodic homogeneous, isotropic turbulence where $N = 32$ and $Re_\Delta \approx 160$ with differential backscatter limiting described in section 4. Spectrum follows closely the K41 scaling $E(k) \sim k^{-5/3}$ over essentially the entire resolved spectrum.

the combination producing the most physical distribution of kinetic energy across all resolved wavenumbers. For the purposes of the free-round jet simulation, the following approach distributed kinetic energy within the resolved scales in closest accordance with classical equilibrium inertial range scalings:

- Non-aliased terms contributing to backscatter are left unchanged. Thus, where a, b and $c \leq 2$,

$$\forall \quad \left(\text{sign}(\gamma)\, x_i^{(a)} x_j^{(b)} x_k^{(c)}\right) \overline{S}_{ij} \geq 0 \quad \Rightarrow \quad C_{\mathcal{B}} = 0.0. \tag{4.2}$$

- Aliased terms contributing to backscatter are completely eliminated. Thus, where a, b or $c = 4$,

$$\forall \quad \left(\text{sign}(\gamma)\, x_i^{(a)} x_j^{(b)} x_k^{(c)}\right) \overline{S}_{ij} \geq 0 \quad \Rightarrow \quad C_{\mathcal{B}} = 1.0. \tag{4.3}$$

- Aliased terms contributing to the forward cascade of energy are amplified. Thus, where a, b or $c = 4$,

$$\forall \quad \left(\text{sign}(\gamma)\, x_i^{(a)} x_j^{(b)} x_k^{(c)}\right) \overline{S}_{ij} \leq 0, \quad \Rightarrow \quad C_{\mathcal{F}} = 3.0. \tag{4.4}$$

- Non-aliased terms contributing to the forward cascade of energy are left unchanged. Thus where, a, b and $c \leq 2$,

$$\forall \quad \left(\text{sign}(\gamma)\, x_i^{(a)} x_j^{(b)} x_k^{(c)}\right) \overline{S}_{ij} \leq 0 \quad \Rightarrow \quad C_{\mathcal{F}} = 0.0. \tag{4.5}$$

As illustrated in Fig. 2, the use of backscatter reduction that varies as a function of term order as described above produces an energy spectrum exhibiting Kolmogorov inertial-range scaling throughout the resolved scales.

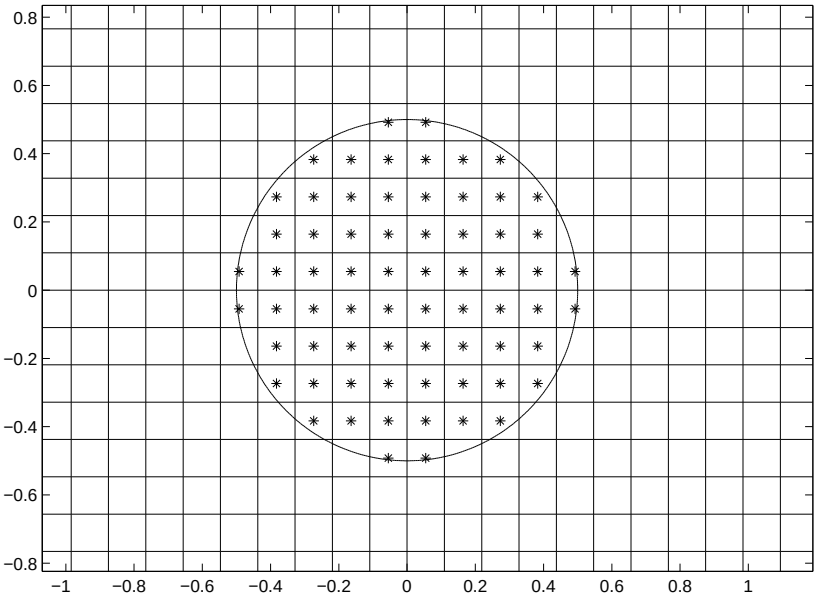

FIGURE 3. Detail of inlet geometry for turbulent jet for $128 \times 64 \times 64$. Cartesian mesh is used to retain the high accuracy of the Legendre interpolation matrices. A physically accurate inlet condition will be established by appropriate volume averaging of the inlet profile for those inlet cells intersecting the maximum inlet radius $D = 7$.

5. LES of a Free Round Turbulent Jet.

5.1. *Configuration and setup.*

Using the refinements to the multifractal subgrid-scale model discussed above in Sections 2 - 4, the structured JETCODE produced at the CTR has been modified to the following configuration to conduct the simulation of the free round turbulent jet. Initial validation simulations are being run at a resolution of $128 \times 64 \times 64$ on a regular Cartesian mesh. The regular mesh has been selected because it allows a single well-conditioned inverse Legendre matrix to be defined throughout the flow domain, which produces exceedingly accurate estimates for the resolved and Δ-scale tensor-product expansions in (2.9) and (2.10). The regular mesh also permits the use of 4th-order centered spatial derivative operators, permitting more accurate determination of the divergence of the backscatter stresses and the related resolved strain-rate fields. Time advancement is with a fully explicit 3rd-order Runge-Kutta scheme. The flow domain is periodic in both cross-stream coordinate directions, and set $\pm 7\,D$ from the centerline, where D is the width of the jet. This configuration has been shown to adequately minimize the impact of the cross-stream periodicity on the downstream development of the jet (da Silva & Métais 2002).

Inflow conditions will consist initially of a core plug flow with constant velocity U_{mean}, and a co-flow in the remainder of the inflow plane of $U_{cf} = 0.1\,U_{mean}$. As illustrated in Figure Fig. 5.1, inlet grid cells intersecting the maximum jet radius (*i.e.*, $r = D$) will contain an appropriate volume-averaged fraction of U_{mean} to ensure accurate implementation of the plug inflow condition. A second inflow condition will also be tested, consisting of the hyperbolic tangent profile (Michalke & Hermann 1982) for the jet core, which has been shown to be a realistic approximation of the actual inlet conditions found in experimental investigations (Freymuth 1966).

This condition is given by

$$U_{mean}(x_o, r) = \frac{U_o + U_{cf}}{2} - \frac{U_o - U_{cf}}{2} \tanh\left[\frac{1}{4}\frac{R}{\theta_o}\left(\frac{r}{R} - \frac{R}{r}\right)\right], \qquad (5.1)$$

where U_o is the centerline jet velocity, U_{cf} is the co-flow velocity and θ_o is the momentum thickness of the initial shear layer.

5.2. *Model evaluation*

Once the initial validation of the modified JETCODE is completed, the accuracy of the multifractal model will be evaluated in direct comparisons with the experimental data of Hussein *et al.* (1994) and others for those statistics traditionally used to evaluate turbulent jet evolution in the self-similar region. These include: (1) linear evolution of jet half-width with downstream location, given by $\delta_{0.5}(x) / D = C_d [\frac{x}{D} - \frac{x_o}{D}]$; (2) decay of the centerline velocity, given by $B_u^{-1} \equiv U_o / \langle u_x(x, r = 0)\rangle$; (3) streamwise-normal mean velocity profiles, given by $(U(r) - U_{cf}) / (U_o - U_{cf})$ as a function of $\eta = r / (x - x_o)$; (4) streamwise-normal Reynolds stress profiles for: streamwise normal stresses $u_x^2 / (U_o - U_{cf})^2$, radial normal stresses $u_r^2 / (U_o - U_{cf})^2$, tangential normal stresses $u_\theta^2 / (U_o - U_{cf})^2$, and streamwise-radial cross stresses $u_x\, u_r / (U_o - U_{cf})^2$; (5) downstream evolution and return to isotropy of the centerline Reynolds stresses $u_x^2(x) / (U_o - U_{cf})^2(x)$. These measures will provide a stringent quantified evaluation of the accuracy of multifractal modeling in the important and complex case of a free round turbulent jet.

5.3. *Additional studies: jet with passive-scalar mixing*

In many combustion problems, such as those arising from the development of systems like the rocket engine, gas turbine and internal combustion engine, the efficient mixing of fuel and oxidizer is accomplished through the use of turbulent jets, whose ability to mix fuel and oxidizer often largely determines the efficiency and stability of the combustion process. LES of such turbulent reacting flows often employ models for local reaction in the subgrid scales that are parameterized by resolved-scale quantities such as the filtered scalar concentrations $\langle\zeta\rangle$, the filtered scalar variance $\langle\zeta'^2\rangle$, and the filtered scalar dissipation rate $\langle 2D\nabla\zeta \cdot \nabla\zeta\rangle$ (See, *e.g.,* Rajagopalan & Tong 2003).

With the completion of the tests described above in section 5.2, the jet flow solver will be augmented with the related multifractal model for the filtered passive-scalar transport equation. That model, whose derivation and initial tests have been described elsewhere in this volume (Burton 2004), uses the multifractal structure of the passive-scalar energy dissipation field in high Reynolds number turbulence to close the filtered passive-scalar transport equation. Tests will compare the accuracy of the model against experimental or DNS data for the behavior of the scalar and scalar dissipation field in the scale-similar region of the jet (Dowling & Dimotakis 1990; Dowling 1991). Statistics to be evaluated will include (1) scale similarity of the normalized scaled concentration field, scalar variance and scalar dissipation rate versus scaled radial component $\eta \equiv r/(x - x_o)$, (2) scaled power spectra for scalar variance and scalar dissipation fields at given downstream and cross-stream locations and (3) probability density functions of scalar concentrations and scalar dissipation rates at the same downstream and cross-stream locations. Such measures will provide a rigorous evaluation of the accuracy of multifractal modeling for turbulent mixing in a complex shear flow seen in a wide range of practical engineering applications.

REFERENCES

BURTON, G. C. 2004 Large-eddy simulation of passive-scalar mixing using multifractal subgrid-scale modeling. *Annual Research Briefs 2004* Center for Turbulence Research, NASA/Stanford University.

BURTON, G. C., & DAHM, W. J. A. 2004 Multifractal subgrid-scale modeling for large-eddy simulation. Part 1: model development and *a priori* testing. *Submitted to Phys. Fluids.*

BURTON, G. C., & DAHM, W. J. A. 2004 Multifractal subgrid-scale modeling for large-eddy simulation. Part 2: backscatter limiting and *a posteriori* evaluation. *Submitted to Phys. Fluids.*

DOWLING, D. R. & DIMOTAKIS, P. E. 1990 Similarity of the concentration field of gas-phase turbulent jets. *J. Fluid Mech.* **218** 109-141.

DOWLING, D. R. 1991 The estimated scalar dissipation rate in gas-phase turbulent jets. *Phys. Fluids A* **9** 2229-2246.

FREYMUTH, P. 1966 On transition in a separated laminar boundary layer. *J. Fluid Mech.* **25**, 683.

HARLOW, F. W. & WELCH, J. E. 1965 Numerical calculation of time-dependent viscous incompressible flow of fluids with free surface. *Phys. Fluids* **8**, 2182-2189.

HUSSEIN, H. J., CAPP, S. P. & GEORGE, W. K. 1994 Velocity measurements in a high-Reynolds-number, momentum-conserving, axisymmetric, turbulent jet. *J. Fluid Mech.* **258**, 31-75.

MICHALKE, A. & HERMANN, G. 1982 On the inviscid instability of a circular jet with external flow. *J. Fluid Mech.* **114** 343.

RAJAGOPALAN, A. G. & TONG, C. 2003 Experimental investigation of scalar-scalar-dissipation filtered joint-density function and its transport equation. *Phys. Fluids* **15** 227-244/

DA SILVA, C. B., & MÉTAIS, O. 2002 Vortex control of bifurcating jets: A numerical study. *Phys. Fluids* **14**, 3798-3819.